Journal of the Optical Society of America B
OPTICAL PHYSICS

Quasi-rotating frame: accurate line shape determination with increased efficiency in noncollinear 2D optical spectroscopy

Patrick L. Kramer, Chiara H. Giammanco, Amr Tamimi, David J. Hoffman, Kathleen P. Sokolowsky, and Michael D. Fayer*

Department of Chemistry, Stanford University, Stanford, California 94305, USA
**Corresponding author: fayer@stanford.edu*

Received 1 March 2016; revised 21 April 2016; accepted 21 April 2016; posted 22 April 2016 (Doc. ID 260334); published 18 May 2016

Multidimensional spectroscopies correlate the oscillation frequencies of an atomic or molecular resonance during at least two different time periods. For two-dimensional (2D) optical spectroscopy, oscillations in the first coherence period are sampled in the time domain point-by-point. We present a general method for accelerating this often lengthy task, the quasi-rotating frame (QRF), through heterodyne detection of the nonlinear signal pulse with a systematic variably delayed local oscillator pulse in a noncollinear (box-CARS) geometry four-wave mixing experiment. 2D infrared (2D IR) vibrational echo experiments are conducted to demonstrate the QRF technique, and the results are compared to data obtained in the stationary frame. We describe straightforward techniques to configure QRF detection, prevent experimental artifacts, appropriately calibrate the rotating frame frequencies, and process the resulting data such that accurate liquid structural dynamics may be extracted from a series of waiting-time-dependent 2D spectral line shapes.

OCIS codes: (320.7150) Ultrafast spectroscopy; (000.2170) Equipment and techniques; (120.5060) Phase modulation; (300.2570) Four-wave mixing.

http://dx.doi.org/10.1364/JOSAB.33.001143

1. INTRODUCTION

Multidimensional spectroscopy is primarily characterized by the presence of more than one time interval between field–matter interactions, if the response is considered in the time domain. When the quantum state of the probed system during a time interval between interactions is a coherent superposition of states with different energies, the quantum state is referred to as a coherence and the time interval is a coherence period [1]. The relative phase between the contributing states oscillates over the interval with their difference frequency, ω, which is directly reflected in the total phase of the final emitted signal with sign depending on the particular interaction pathway. Population states also occur, in which the system is characterized by an eigenstate; the quantum state does not exhibit oscillations.

Third-order nonlinear optical spectroscopy with femtosecond pulses, in frequency ranges from the infrared (IR) through the visible and ultraviolet (UV), has proven to be an incisive tool for investigating the ultrafast dynamics of complex condensed matter systems [2–12]. The third-order nonlinear response functions for two-dimensional (2D) vibrational or photon echo spectroscopies consist of a first coherence period, population period, and second coherence period separating the four field–matter interaction events (three input pulses stimulate the emission of a signal pulse) [1,13]. One of the most widely used schemes for sampling this response function to measure ultrafast dynamics is a mixed time- and frequency-domain approach [14–18]. The final coherence period, in which the nonlinear signal is emitted, is Fourier transformed by a monochromator (configured as a spectrograph), and the dispersed signal is detected on a multichannel array or camera, reading out all final emission frequencies of interest simultaneously. For the initial coherence period, the sampling is instead done in the time domain. The delay between the first two pulses is varied while keeping the pulse 2 to 3 delay fixed, with the resulting phase oscillations of the signal recorded through optical heterodyne detection by interference with a temporally fixed local oscillator (LO) pulse. Experiments are conducted with different fixed population periods between the two coherence periods to map out the dynamic changes in the system. Because there are no coherent oscillations, the sampling considerations for the population time are not very stringent.

Constructing a 2D correlation spectrum with the first coherence period determining the initial frequency axis, however, requires interferometric precision in the time delays and sufficient time point sampling to at least satisfy the Nyquist condition for unambiguous assignment of the oscillation

frequencies. For the relatively long dephasing times [up to several picoseconds (ps)] and short optical periods [usually less than 20 femtoseconds (fs)] often encountered for vibrational or electronic transitions, adequately sampling the first coherence period until its complete decay is commonly the most time-consuming part of 2D optical spectra acquisition. Systematic under sampling is one approach that can reduce the number of points that need to be acquired, but then the sampling rate must be carefully chosen to avoid aliasing of unwanted features onto the desired signal [13].

Most phenomena and techniques encountered in coherent optical spectroscopy have analogs in nuclear magnetic resonance (NMR) [19]. In NMR, sampling of coherence periods is naturally accomplished in the rotating frame, that is, a frame that oscillates in phase in such a way as to cancel much of the phase progression that would be observed in a directly detected sample response [20]. This results from the excitation pulses having a phase that also varies as the coherence time delay is stepped; the radio frequency pulses used in NMR sequences are arbitrarily shaped in phase and amplitude by the spectrometer electronics from a common carrier wave [21]. With advances in Fourier-domain optical pulse shaping technology, the generation of collinear laser pulse trains of arbitrarily shaped pulses has become accessible [13,22–26]. In particular, the relative phase of the first pulse pair can be varied with each time step giving rise to a frequency of the user's choice, the rotating frame frequency, ω_f. This results in the apparent frequency of oscillation during the first coherence time appearing at $\omega - \omega_f$. One obtains a spectrum with the same information content (provided ω_f is known), but less densely spaced time points are required.

In many implementations of 2D optical spectroscopy, however, the pulse sequence is generated noncollinearly with precisely set variable path lengths to control the pulse delays [9,14,15,27,28]. There are certain advantages to these setups, such as independent control of all pulse polarizations and more straightforward manipulation of the LO separately from the signal to optimize their intensity ratio for the highest signal to noise possible. However, the pulse phases are not usually controllable other than through time delays, which can approximate phase shifts relatively well for small time steps at a particular frequency, but yield quite different results at different frequencies for delays equivalent to several cycles and beyond [21]. Manipulation of the excitation pulse phases (through delays) to bring the coherence period oscillations into a rotating frame is thus not possible in the fully noncollinear geometry. Time shifts of the excitation pulses cannot satisfactorily compensate phase evolution when the phase changes are originally due to these specific delays in the sampling of the nonlinear response functions.

In partially collinear (pump–probe) geometry experiments, the final excitation pulse also serves as the LO, so the signal-LO relative phase is fixed. The LO is an independent pulse in the noncollinear experiments. In this paper, we show how the detection in the noncollinear geometry can be brought into a partially rotating frame using variable LO delays in sync with the first coherence period sampling. Engel's group has noted the occurrence of such a rotating frame previously [29–32]. In the collection of single shot 2D electronic spectra using the Gradient Assisted Photon Echo Spectroscopy (GRAPES) technique, a pulse-front tilt between the first and second beams, focused to stripes rather than spots, is used to encode the first coherence time spatially. The direction of the LO stripe that is collinear with the emitted signal results in a time delay between the signal and LO pulses that varies along with the first coherence time spatially. The 2D spectra appear in a rotating frame [30]. However, this method only works for systems in which the time range of the first coherence period is short, e.g., less than 1 ps. Other approaches to phase-stabilized 2D electronic spectroscopy using scanned delay stages similarly resulted in rotating frame detection because the increments in the first coherence time delay and pulse 3–LO delay are locked to one another [33–35].

These experimental designs result in fully rotating frame detection for the first coherence time, which has the most relaxed sampling constraint because the signal appears centered at zero frequency. As discussed in Section 2.C, however, the positive and negative frequency components contributing to the first coherence time oscillations interfere with each other if further steps to isolate only one contribution are not taken. The locations of the various peaks of interest and overall amplitude features such as coherent oscillations will likely not be affected adversely. However, the precise line shapes, from which detailed solvent fluctuation dynamics are extracted, can be disrupted by these interferences. A partially rotating frame, where the signal oscillates at a reduced frequency that is still above zero, is preferable for the extraction of accurate line shape details.

In this paper, we present a new technique, the quasi-rotating frame (QRF), which operates similarly to the rotating frame present in GRAPES but is usable with standard scanned-acquisition noncollinear 2D spectrometers. Furthermore, by appropriate choice of the delay programming, the user can choose to shift the signal into any partially rotating frame desired without the geometric constraints that define the GRAPES rotating frame frequencies. In most existing noncollinear 2D spectrometers the LO pulse is delayed relative to the third excitation pulse and nonlinear signal with a computer-controlled precision delay stage to initially set the temporal overlap with the signal, and possibly to adjust for drift over long experiments using a feedback loop [36]. This ability to vary the LO delay fairly rapidly and precisely is the only requirement for using the QRF. Existing systems meeting these requirements need only minor software changes for its implementation.

The details of our QRF implementation and the necessary data processing are discussed in Section 2, following an overview of heterodyne detected noncollinear third-order experiments. In Section 3, the technique is illustrated using two-dimensional infrared (2D IR) vibrational echo experiments with both short-pulse broad-bandwidth and longer-pulse narrower-band spectrometer setups. While the QRF is clearly effective and functional in both cases, its use with narrow absorption features allows more improvement over the stationary frame than with broader absorptions. A brief guide to the configuration of QRF detection is given in Section 4, summarizing the major points of the previous sections for quick reference by experimenters. Concluding remarks appear in Section 5. Because certain heterodyne scatter terms that did not contribute oscillations in the stationary frame do oscillate with QRF detection enabled,

a brief overview of the quasi-phase-cycling (QPC) routine [37] we use to remove this scatter is given Appendix A.

2. THIRD-ORDER 2D SPECTROSCOPY AND THE QRF PROCEDURE

A. Heterodyne-Detected Third-Order Signals

In a third-order noncollinear time-domain wave-mixing experiment, three variably time-ordered excitation pulse fields E_1, E_2, and E_3 cross in the sample with the unique wave vectors $\vec{k}_1$, $\vec{k}_2$, and $\vec{k}_3$. The time intervals, shown in Fig. 1, are t_1 between pulses 1 and 2 (the first coherence period), t_2 between pulses 2 and 3 (the population period or waiting time), and t_3 for signal emission following pulse 3 (the second coherence period). We consider the nonlinear signal E_s emitted in the $\vec{k}_s = -\vec{k}_1 + \vec{k}_2 + \vec{k}_3$ phase-matched direction, which is overlapped spatially with a fourth pulse, the LO, that does not pass through the sample. The local oscillator field E_{LO} serves to amplify the weak signal and provide phase resolution through optical heterodyne detection [1,13,14].

In many 2D optical spectroscopy experiments (particularly in the infrared spectral regime, which we shall focus on as an example for the remainder of the paper), the LO is made temporally coincident with the signal pulse. The signal is emitted beginning with the arrival of pulse 3, that is, from $t_3 = 0$ [13]. Although the LO does not pass through the sample as pulses 1–3 do, we shall refer to the LO pulse delay relative to pulse 3, t_{LO}, with the definition that $t_{\mathrm{LO}} = 0$ when the LO and signal pulse are temporally coincident at $t_1 = 0$ (this ensures the signal is emitted from $t_3 = 0$ even if an echo would occur for positive t_1). If the LO did pass through the sample (as in some implementations of noncollinear 2D optical spectroscopy), t_{LO} defined in this sense would in fact be the LO delay from pulse 3.

For simplicity we consider a single band in the 2D IR spectrum: the 0-1 peak on the diagonal with average frequency

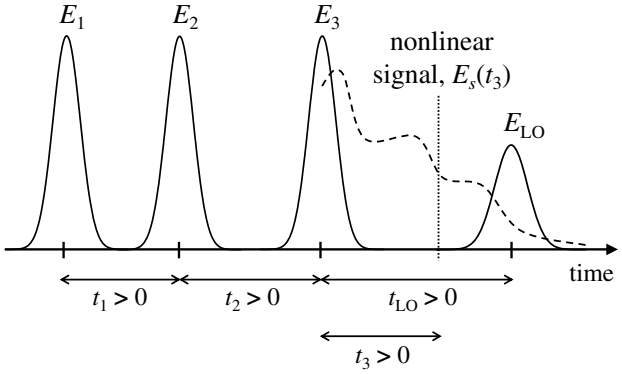

Fig. 1. Illustration of the pulse sequence for third-order nonlinear optical experiments, such as 2D IR spectroscopy. Three excitation pulse fields E_1, E_2, and E_3 interact with the sample and generate the nonlinear signal, which is heterodyned by the fourth pulse, E_{LO} (field envelopes are shown). The experimentally controlled time delays are t_1, the first coherence time, t_2, the waiting time, and t_{LO}, the local oscillator delay. The signal field E_s (dashed curve) is emitted following the third pulse throughout the final coherence time, t_3. A particular value of t_3 is illustrated at the vertical dotted line. Pulse time orderings are shown such that all the time intervals are positive.

$\langle\omega_{10}\rangle$ and instantaneous frequency fluctuation $\delta\omega_{10}(t) = \omega_{10}(t) - \langle\omega_{10}\rangle$. Additional spectral features, such as the 1–2 transition that is commonly observed in 2D IR, can be treated entirely analogously. Furthermore, we ignore the effect of finite excitation pulse duration using the semi-impulsive limit, i.e., the electric field only interacts with the system at the exact center of each pulse in time [1,13]. In this case the third-order nonlinear signal as a function of the three time delays, t_1, t_2, and t_3, is proportional to the total third-order response function, $R^{(3)}(t_1, t_2, t_3)$ (the sum of response functions for all contributing pathways). This approximation greatly simplifies the form of the nonlinear signal allowing us to directly motivate and describe the QRF procedure. The basic features of the analysis remain unchanged in the case in which the nonlinear signal is given by a time-ordered triple integral over the product of the excitation fields with the response function [1]. We are concerned primarily with the phase changes due to moving the pulse centers in time, not the effects of pulse duration on the precise line shapes observed [1,13,38,39].

We make use of the semiclassical approximation to neglect differences in ground-state bleach and excited-state absorption pathways, which are usually indistinguishable for IR transitions. Furthermore, reorientation and population decay will not be included. They can be incorporated as multiplicative factors to the response functions. When the three excitation pulses are not overlapping, there are two classes of excitation pathways for the third order observable in 2D IR spectroscopy (in which pulse 3 arrives last): the rephasing (RP) and nonrephasing (NR) pathways. The rephasing signal is obtained in the phase-matched direction when the pulse arrival order is 1, 2, 3. The nonrephasing signal is emitted in a different direction, $\vec{k}_1 - \vec{k}_2 + \vec{k}_3$, with this ordering. However, if the pulse arrival order is 2, 1, 3 instead, the nonrephasing signal is obtained in the normal phase-matched direction. This leads to the conventional "dual-scan" method for obtaining absorptive 2D IR spectra (requiring the sum of RP and NR response functions) [13,15,17,27]. The response functions, without making either the Condon or second cumulant truncation approximations [1,40], are for rephasing

$$R^{(3)}_{\mathrm{RP}}(t_1, t_2, t_3) = \exp(+i\langle\omega_{10}\rangle t_1 - i\langle\omega_{10}\rangle t_3) \times \langle\mu_{10}(0)\mu_{10}(t_1)\mu_{10}(t_1 + t_2) \times \mu_{10}(t_1 + t_2 + t_3)\phi_{\mathrm{RP}}(t_1, t_2, t_3)\rangle \quad (1)$$

and for nonrephasing

$$R^{(3)}_{\mathrm{NR}}(t_1, t_2, t_3) = \exp(-i\langle\omega_{10}\rangle t_1 - i\langle\omega_{10}\rangle t_3) \times \langle\mu_{10}(0)\mu_{10}(t_1)\mu_{10}(t_1 + t_2) \times \mu_{10}(t_1 + t_2 + t_3)\phi_{\mathrm{NR}}(t_1, t_2, t_3)\rangle, \quad (2)$$

where $\mu_{10}(t)$ is the transition dipole magnitude and

$$\phi_{\mathrm{RP}}(t_1,t_2,t_3) = \exp\left[i\int_0^{t_1} \mathrm{d}\tau\delta\omega_{10}(\tau) - i\int_{t_1+t_2}^{t_1+t_2+t_3} \mathrm{d}\tau\delta\omega_{10}(\tau)\right],$$
$$\phi_{\mathrm{NR}}(t_1,t_2,t_3) = \exp\left[-i\int_0^{t_1} \mathrm{d}\tau\delta\omega_{10}(\tau) - i\int_{t_1+t_2}^{t_1+t_2+t_3} \mathrm{d}\tau\delta\omega_{10}(\tau)\right]. \quad (3)$$

The line shape is determined in Eqs. (1) and (2) by the ensemble averages (four-time correlation functions) over the transition dipoles and ϕ factors of Eq. (3), while the position of the 2D spectral features in a frequency domain representation is set by the phase factors involving the average frequency in the first lines of Eqs. (1) and (2).

The rephasing and nonrephasing pathways differ in the sign of their phase evolution during the first coherence period, t_1. It will simplify the discussion to rearrange these expressions to more closely model the form of the data as it is collected experimentally. Although the response functions are only defined for $t_i \geq 0$, it is conventional to report the first coherence time as a negative t_1 if pulse 2 precedes pulse 1. The nonnegative population time t_2 is the delay between pulses 1 and 3 in this case, and the meaning of t_3 is unchanged. Then we can define a new response function,

$$\begin{aligned} S^{(3)}(t_1, t_2, t_3) = &\exp(+i\langle\omega_{10}\rangle t_1 - i\langle\omega_{10}\rangle t_3) \\ &\times \langle\mu_{10}(0)\mu_{10}(|t_1|)\mu_{10}(|t_1| + t_2) \\ &\times \mu_{10}(|t_1| + t_2 + t_3)\phi_s(|t_1|, t_2, t_3)\rangle, \end{aligned} \quad (4)$$

where $\phi_s = \phi_{\mathrm{RP}}$ for $t_1 \geq 0$ and $\phi_s = \phi_{\mathrm{NR}}$ for $t_1 < 0$. Equation (4) simply encodes both the RP and NR time-ordered responses as a single function. In particular, note that the t_1-dependent phase on the first line of Eq. (4) has the same form for either pathway. If, for instance, t_1 is scanned from its maximum negative value (i.e., maximum positive delay from pulse 2 to pulse 1), through zero (pulses 1 and 2 coincident), and finally to its maximum positive value (delay from pulse 1 to 2), the phase on $S^{(3)}$ increases uniformly with t_1, and with an opposite sign to the oscillation frequency of the emitted signal in t_3.

As mentioned above, the signal field (oscillating in real time, t_3) is proportional to the response function in the semi-impulsive limit,

$$E_s(t_3) \propto S^{(3)}(t_1, t_2, t_3), \quad (5)$$

for particular values of t_1 and t_2. The local oscillator pulse field for heterodyne detection is written as $L(t)$, where the envelope of L is peaked at $t = 0$. When delayed relative to pulse 3 as shown in Fig. 1 and discussed above, the LO field is

$$E_{\mathrm{LO}}(t_3) = L(t_3 - t_{\mathrm{LO}}). \quad (6)$$

The emitted nonlinear signal is Fourier transformed by a monochromator to give a frequency-domain representation, written as

$$\begin{aligned} \tilde{E}_s(\omega_3) &= \tilde{S}^{(3)}(t_1, t_2, \omega_3) \\ &= \int_{-\infty}^{\infty} \mathrm{d}t_3 \, \exp(i\omega_3 t_3) S^{(3)}(t_1, t_2, t_3). \end{aligned} \quad (7)$$

The spectrum of the nondelayed ($t_{\mathrm{LO}} = 0$) LO is

$$\tilde{L}(\omega_3) = \int_{-\infty}^{\infty} \mathrm{d}t_3 \, \exp(i\omega_3 t_3) L(t_3), \quad (8)$$

from which we obtain

$$\tilde{E}_{\mathrm{LO}}(\omega_3) = \exp(i\omega_3 t_{\mathrm{LO}}) \tilde{L}(\omega_3) \quad (9)$$

by the Fourier shift theorem.

When the signal and LO beams are spatially overlapped and mode-matched, the response (e.g., a voltage) produced by a square-law detector after the monochromator is given by

$$V = |\tilde{E}_s(\omega_3) + \tilde{E}_{\mathrm{LO}}(\omega_3)|^2, \quad (10)$$

up to some proportionality constant. The homodyne nonlinear signal term, $|\tilde{E}_s|^2$, is generally much smaller than the LO intensity, $|\tilde{E}_{\mathrm{LO}}|^2 = |\tilde{L}|^2$, and can be neglected in the expansion of Eq. (10). If one excitation beam is chopped to remove the nonlinear signal on alternate laser shots, the LO intensity spectrum can be subtracted to isolate the heterodyne term,

$$\begin{aligned} V_H &= 2\mathrm{Re}(\tilde{E}_s(\omega_3) \times \tilde{E}^*_{\mathrm{LO}}(\omega_3)) \\ &= 2\mathrm{Re}(\tilde{E}_s(\omega_3)\tilde{L}^*(\omega_3)\exp(-i\omega_3 t_{\mathrm{LO}})) \equiv 2\mathrm{Re}(C). \end{aligned} \quad (11)$$

The complex cross term is defined here as C. The spectrum $\tilde{L}$ is independent of t_{LO}, so the entire effect of the LO delay in Eq. (11) is captured by the phase factor on the second line. It results in a heterodyne term with oscillations in ω_3 when $t_{\mathrm{LO}} \neq 0$ is fixed, referred to as a spectral interferogram [16]. Alternatively, at a fixed ω_3, one obtains a temporal interferogram as t_{LO} is varied (Section 2.D).

We shall focus in particular on the complex cross term C in Eq. (11), noting that the final signal will be given by twice its real part. The cross term is rewritten as

$$\begin{aligned} C &= \tilde{S}^{(3)}(t_1, t_2, \omega_3)\tilde{L}^*(\omega_3)\exp(-i\omega_3 t_{\mathrm{LO}}) \\ &= \exp(i\langle\omega_{10}\rangle t_1 - i\omega_3 t_{\mathrm{LO}})\Phi^{(3)}(t_1, t_2, \omega_3)\tilde{L}^*(\omega_3). \end{aligned} \quad (12)$$

Here $\Phi^{(3)}$ has been defined as the t_3 Fourier transform (FT) of $\exp(-i\langle\omega_{10}\rangle t_1)S^{(3)}(t_1, t_2, t_3)$ [see Eq. (4)]. We have factored out the t_1 phase evolution from the rest of the response function. The $\Phi^{(3)}$ factor determines the complete ω_3 spectrum and the ω_1 line shape (centered at $\omega_1 = 0$ rather than $\langle\omega_{10}\rangle$) of the third-order signal.

B. Sampling and the Generation of Quasi-Rotating Frame Heterodyne Signals

At a fixed population time (or waiting time) t_2, a 2D spectrum can be generated by scanning t_1 and numerically Fourier-transforming the resulting interferogram obtained from the heterodyne voltage in Eq. (11):

$$\tilde{A}(\omega_1, t_2, \omega_3) = \int_{-\infty}^{\infty} \mathrm{d}t_1 \exp(-i\omega_1 t_1) V_H(t_1, t_2, \omega_3, t_{\mathrm{LO}}). \quad (13)$$

To unambiguously determine the ω_1 spectra from this interferogram, it must be sampled at a high enough rate in t_1. Suppose that the highest frequency contributing to the initial excitation of the vibrational probe in $\omega_1/2\pi$ is $B = 3000\ \mathrm{cm}^{-1}$. Then the signal is contained in a total bandwidth (including all positive and negative frequencies, from $-B$ to B) of $2B = 6000\ \mathrm{cm}^{-1}$. By the Nyquist–Shannon sampling theorem, the t_1 point spacing must be less than $\Delta t = 1/(2B \times c) = 5.6$ fs to avoid aliasing. This is equivalent to the requirement that the sampling interval must be less than half of the $3000\ \mathrm{cm}^{-1}$ temporal period of 11.2 fs.

If by some means the signal were made to oscillate with no frequencies higher than, for example, $B = 500\ \mathrm{cm}^{-1}$ instead, the maximum point spacing becomes $\Delta t = 33.3$ fs, 6 times larger. Because each sampled t_1 point requires movement of

a precision mechanical translation stage and some waiting for it to settle to within a few tens of nanometers in real space, a few times reduction in the point sampling can result in considerably faster data acquisition, even if more laser shots are accumulated at each t_1 to result in the same total number of shots.

The QRF procedure shifts nonlinear signals into a rotating frame in t_1 to decrease the effective oscillation frequency as described in the following. We have assumed that t_{LO} can be arbitrarily changed with high precision during the course of an experiment, just like t_1 and t_2. Let f, with $0 \le f \le 1$, be defined as the "QRF fraction." We choose $t_{LO} = f \times t_1$ as the variable LO delay. Thus the LO is delayed to a fraction f of t_1 later than pulse 3 for positive t_1 (rephasing signal), and is moved in advance of pulse 3 by the fraction f of $|t_1|$ for negative t_1 (nonrephasing signal); see Fig. 1. From Eq. (12), we find

$$\begin{aligned} C &= \exp(i\langle\omega_{10}\rangle t_1 - if\omega_3 t_1)\Phi^{(3)}(t_1, t_2, \omega_3)\tilde{L}^*(\omega_3) \\ &= \exp(i(\langle\omega_{10}\rangle - f\omega_3)t_1)\Phi^{(3)}(t_1, t_2, \omega_3)\tilde{L}^*(\omega_3). \end{aligned} \quad (14)$$

It can be seen that the center frequency of the nonlinear signal in ω_1 has been shifted from $\langle\omega_{10}\rangle$ to $\langle\omega_{10}\rangle - f\omega_3$. The rotating frame frequency $\omega_f = f\omega_3$ depends on the monochromator frequency at which the temporal interferogram in Eqs. (11) and (12) is being recorded.

The effect of QRF detection on the recorded 2D spectral range is easy to understand when viewed graphically, as in Fig. 2. A rectangular range of interest as would be collected in the stationary frame is shown in Fig. 2(a). The initial and final limits are encoded as "i" and "f", respectively, e.g., $\omega_{3,f}$ is the upper (final) limit in the ω_3 axis. With QRF detection and a fraction f, the range is transformed to the parallelogram shown in Fig. 2(b) [note that the ω_1 axis is not the same in parts (a) and (b) of the figure]. While the ω_3 limits are assumed unchanged, the previously vertical ω_1-edges of the range obtain a slope of $-1/f$. Similarly, the slope of the diagonal (dotted line) becomes $1/(1-f)$. To analyze the 2D line shapes of spectral features, it is clearly critical to accurately correct for the ω_3-dependent rotating frame frequency to undo the skew of the spectral range.

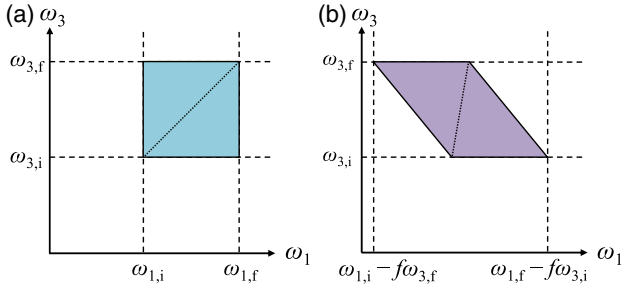

Fig. 2. Geometric representation of the observed range in frequency space in 2D optical spectra. (a) Stationary frame, sampled region filled (blue). Dashed lines show the ω_1 and ω_3 initial (i) and final (f) limits. The limits for both axes are commonly equal, but need not be, for single-color spectroscopies. The dotted line is the diagonal, $\omega_3 = \omega_1$. (b) Quasi-rotating frame (QRF) with fraction f. The sampled rectangle from (a) is transformed to the filled parallelogram (purple). Limits in ω_3 are unchanged, but the range in ω_1 is increased by $f(\omega_{3,f} - \omega_{3,i})$ as the oscillation frequencies are lowered by $f\omega_3$. The diagonal line is now described by $\omega_1 = (1-f)\omega_3$.

The two most important "vertical" ω_1 limits in the rotating frame are also shown in Fig. 2(b). Stationary frame features from Fig. 2(a) appear at the lowest frequency in Fig. 2(b) at $\omega_{1,i} - f\omega_{3,f}$ and at the highest frequency of $\omega_{1,f} - f\omega_{3,i}$. The high-frequency limit of course determines the reduction in sampling that is possible for a given f and ω_3 range of interest. The rectangular region of Fig. 2(b) within the dashed bounds must be fully sampled (assuming that each ω_3 channel is obtained simultaneously) and entirely within the positive-frequency half of ω_1 to correctly reconstruct the blue region of Fig. 2(a); the lower limit will be discussed further below.

C. QRF Practical Aspects and Challenges

In the preceding Section 2.B, the QRF procedure was described in mathematical completeness for an idealized situation. Acquisition of real data with the QRF requires some additional considerations. In this section we identify several challenges that arise in the course of obtaining correct 2D spectral line shapes with the QRF. We have found straightforward solutions to all the challenges; they are described in this and subsequent sections.

First, the movements of the delay lines determining t_1, t_2, and t_{LO}, while accurate and reproducible, cannot be chosen arbitrarily. Distance traveled must be a multiple of the minimum step size (10 nm, for example). Once a compatible sampling interval Δt in t_1 is chosen, the QRF fraction f can no longer be chosen independently. The requirement is that $f\Delta t$ is also obtainable by an integer number of delay line steps. Typically one first chooses a rough f value, from which an optimal sampling rate is derived. Then, the closest f value that is consistent with the sampling rate and delay line motion is computed and used to actually acquire the QRF interferogram. As long as this true f is known, the rotating frame spectrum can be accurately shifted up to stationary frame frequencies.

Much of the above discussion focused on the complex cross-term C in Eq. (11), which contains only positive frequencies in ω_1 [with the t_1 FT defined in Eq. (13)]. The heterodyne detected interferogram V_H is actually twice the real part of C, so the FT shown in Eq. (13) to obtain a 2D correlation spectrum will contain both positive and negative ω_1 frequencies. The QRF procedure shifts both the positive and negative frequency components toward zero frequency. This is illustrated in Fig. 2 for the positive frequencies; the negative frequency half is a mirror image across $\omega_1 = 0$. Larger values of f shift the lowest oscillating frequency in the range of Fig. 2(b) closer to zero. This progression sets a limit on how large f can be, because eventually the positive and negative frequency components will be shifted past zero and will overlap and interfere with each other. They cannot be separated in this case and reconstruction of the stationary frame spectrum will not be possible. Thus, if $\omega_{1,i}$ is the lowest initial oscillation frequency in the stationary frame spectrum, and $\omega_{3,f}$ is the highest final oscillation frequency detected, then f must be chosen such that

$$\omega_{1,i} - f\omega_{3,f} > 0. \quad (15)$$

As long as the inequality above is satisfied, f can be chosen as large as desired to minimize the oscillation frequencies that are sampled.

With QRF sampling as described to this point, only a partially rotating frame allows reconstruction of the normal spectrum. Certain phase cycling schemes can, in fact, remove the negative frequency half of the ω_1 spectrum, allowing detection in the fully rotating frame. This has been demonstrated using pulse shaping techniques in 2D IR spectroscopy [22,23,41]. In principle, using an analogous QPC routine, fully rotating frame detection could be accomplished in the noncollinear geometry considered in this work. However, even when enabled by a pulse shaper, the partially rotating frame is often superior because the technical noise (see below) appearing near zero frequency can be larger than at positive, but still relatively low frequencies [22,23]. Thus, working in a partially rotating frame is actually the ideal operating regime for the QRF.

Phase cycling can provide additional benefits in the acquisition of real signals with the QRF. When pulses 1 and 2 are variably delayed to produce t_1 interferograms, it is pulse 3 that is chopped on alternate laser shots. If a sample of imperfect optical quality is used, all three excitation beams can contribute scattered light in the signal direction. The scatter that interferes with the LO and therefore depends on the phase of beams 1 or 2 (appearing on the diagonal in the frequency domain) is removed by chopping. Beam 3 scatter remains, but it does not oscillate rapidly in the stationary frame and thus does not interfere greatly with the 2D spectrum, which appears at high frequencies [Fig. 2(a)]. In the rotating frame, however, the beam 3 scatter that is heterodyned by the LO will rapidly oscillate as the LO phase varies with the t_{LO} delay. This term, along with several others, is selected against in our implementation of the QRF by a QPC [37] procedure in which the pulse 1 and 2 delays are varied in half-cycle steps by the precision delay lines. The QPC implementation details are given in Appendix A.

The laser system, mechanical, and electronic components of the 2D spectrometer can all contribute noise that is detected on top of the desired optical signals. The noise appears in the interferogram, and its real-time amplitude variation is mapped onto the coherence time sampling rate we choose. Based on the spectral characteristics of the noise, it will appear at a particular frequency (or range of frequencies) when the interferogram is Fourier transformed. The location depends on the true noise spectrum, the chosen t_1 sampling rate, and the real time interval between the collection of data at t_1 points. The apparent frequencies of the noise are often lower than the IR frequencies of interest, but these artifacts are also shifted into the stationary frame in the postprocessing of QRF data. In the stationary frame case, such noise peaks still exist in the spectrum but are far redshifted from the ω_1 range of interest. Depending on the behavior of the particular 2D optical spectroscopy system, certain regions of ω_1 should be avoided to keep the desired peaks from overlapping with artifacts from noise. If a particular f value is found to place the peak of interest in a noisy spectral region, often a small change in f can shift the peak to a cleaner ω_1 location.

Reconstructing the stationary frame 2D IR spectrum from QRF data requires knowledge of the exact value of f and the ω_3 frequencies at which the data were collected. Error in the precise LO pulse delay times t_{LO} can lead to an effectively different f than the one used to choose the number of LO delay line steps to take with each t_1, t_{LO} move. While mildly imperfect monochromator calibration can result in a slight distortion of the ω_3 axis, the line shape features (e.g., center line slope (CLS) method for obtaining the frequency–frequency correlation function (FFCF) [38,42]) will not change appreciably in the stationary frame. However, if these ω_3 values are used to shift QRF data to the stationary frame, significant distortion can remain that does change the CLS because the skew of the entire spectrum varies [Fig. 2(b)]. It is therefore vital to determine the exact rotating frame frequency that will be produced at each ω_3(each pixel of the array detector) for a given $f\Delta t$ step size in t_{LO}. The solution to this challenge is described in Section 2.D.

A final aspect that distinguishes real QRF detection from the idealization of Section 2.B is the finite frequency resolution of the ω_3 detection. If only a single, infinitely sharp, frequency is isolated by a monochromator, the time-domain representations of the signal and local oscillator fields are infinitely long-lived. However, monochromators do not have perfectly sharp frequency resolution, and the dispersed light field is detected on an array or camera with pixels of finite width. Each pixel delivers a response proportional to the power in a spectral range. The signal and LO electric fields in this spectral range do have a limited extent in time, and delaying the LO pulse relative to the signal pulse causes them to overlap over less of their temporal widths, which lessens the depth of modulation in heterodyne detection. Thus as t_1 and t_{LO} are scanned, the interferogram envelope decays more rapidly than in the stationary frame; this is a form of apodization. For long t_1 (and therefore t_{LO}) ranges, the temporal walk-off of the signal and LO pulses is most apparent. To recover the correct width in ω_1 for the reconstructed spectrum when this effect is prominent, we must take account of this apodization (i.e., antiapodize using the inverse envelope decay). Both the apodization function and calibration of the rotating frame frequencies can be addressed through an additional experiment, the calibration interferogram.

D. Calibration Interferogram

We need to isolate the phase evolution and envelope decay of the heterodyne signal, Eq. (11), due to the varying delay of the LO pulse relative to the signal. It will be shown that the interferogram produced by scanning the LO time delay t_{LO} through the range of interest (i.e., longer than f times the t_1 range) with all other times fixed carries the necessary information on the rotating frame frequencies and envelope decays. This experiment is referred to as the (array) calibration interferogram.

Let $P_k(\omega)$ be the voltage response of pixel k to light intensity of frequency ω, which is governed by the spectral characteristics of the photosensitive material, the pixel size, and the monochromator characteristics (e.g., grating line density, angles). In particular, P_k is strictly zero for positive frequencies outside the range $\omega_{k,i} < \omega < \omega_{k,f}$ (light frequencies outside this range do not hit the pixel at all) and the response center is ω_k. Negative frequencies are not treated any differently from

positive: P_k must be an even function. The pixel k response to the heterodyne signal V_H in Eq. (11) is thus

$$V_{H,k}(t_{\mathrm{LO}}) = \int_{-\infty}^{\infty} \mathrm{d}\omega_3 P_k(\omega_3) V_H(t_1, t_2, \omega_3, t_{\mathrm{LO}}), \quad (16)$$

where we have made the dependence on t_1 and t_2 implicit, as these will be held constant in this discussion of calibration. The integration limits are arbitrary as long as they are outside the total range of P_k; it proves quite useful to set them to plus and minus infinity.

The signal and LO electric fields are real functions of time (when all response functions are included [1]), so the LO spectrum must obey $\tilde{L}(-\omega) = \tilde{L}^*(\omega)$, and similarly for the signal. Thus from Eqs. (11) and (16) we obtain

$$\begin{aligned} V_{H,k}(t_{\mathrm{LO}}) &= \int_{-\infty}^{\infty} \mathrm{d}\omega_3 P_k(\omega_3)[\tilde{E}_s(\omega_3)\tilde{L}^*(\omega_3)\exp(-i\omega_3 t_{\mathrm{LO}}) \\ &\quad + \tilde{E}_s^*(\omega_3)\tilde{L}(\omega_3)\exp(+i\omega_3 t_{\mathrm{LO}})] \\ &= 2\int_{-\infty}^{\infty} \mathrm{d}\omega_3 \exp(-i\omega_3 t_{\mathrm{LO}}) P_k(\omega_3)\tilde{E}_s(\omega_3)\tilde{L}^*(\omega_3), \end{aligned} \quad (17)$$

where the second line was obtained by replacing $\omega_3 \rightarrow -\omega_3$ in the first line's second term and using the properties of the field spectra and pixel response discussed above. Then the calibration interferogram is simply twice the FT of $P_k(\omega)\tilde{E}_s(\omega)\tilde{L}^*(\omega)$. The power spectrum of the interferogram $V_{H,k}$ is

$$\begin{aligned} I(\omega) &= \left| \int_{-\infty}^{\infty} \mathrm{d}t_{\mathrm{LO}} \exp(i\omega t_{\mathrm{LO}}) V_{H,k}(t_{\mathrm{LO}}) \right|^2 \\ &= 2P_k^2(\omega_3)|\tilde{E}_s(\omega_3)|^2|\tilde{L}(\omega_3)|^2. \end{aligned} \quad (18)$$

Thus we obtain $P_k(\omega)^2$ times the intensity spectra of the signal and LO.

The power spectrum, Eq. (18), is the key piece of information in calibrating the rotating frame frequencies. Intensity spectra of the signal and LO can often be considered spectrally flat compared to the narrower pixel width. If not, $I(\omega)$ can simply be divided by the signal and LO intensity spectra. This power spectrum can be used to obtain the pixel center ω_k through a variety of analysis methods. While the true pixel response is likely to have a somewhat flat top, the calibration interferogram is not usually taken for long enough t_{LO} delays that the amplitude has dropped to zero. Thus the FT in Eq. (18) will be convolved with the transform of the time-domain window (i.e., a sinc function from the rectangular window), making the pixel response appear much more peaked. We find that apodizing the calibration interferogram with a Hann window results in a cleaner power spectrum. The ω location of the peak in Eq. (18) is determined by picking the maximum value of $I(\omega)$, and this point is identified as the pixel center ω_k.

If the LO delay line step size is known accurately, this pixel-center determination is an expedient way to determine the calibration of a monochromator and array detector with sufficient accuracy, and ensure the recorded ω_3 frequency values are the correct ones so that QRF data can be properly shifted to the stationary frame. Simultaneously checking the actual frequency recorded on each pixel versus the calculated frequency (based on the monochromator dimensions and array or camera positioning) can also be quite helpful in positioning the detector initially or correcting for nonideal behavior in the monochromator drive hardware.

Even if the LO is delayed by unknown but reproducible time steps, the effective frequencies obtained from the interferogram are still precisely those "ω_3" values needed to obtain the rotating frame frequencies $f\omega_3$. Then they simply do not correspond to the true detected monochromator frequencies on the vertical axes of Fig. 2. Thus, one can still use QRF detection when the beam direction into the LO delay path is misaligned, or with uncalibrated but precise means of generating a delay (e.g., translatable glass wedge pairs [28]). Given that the monochromator is calibrated, recording the calibration interferogram provides a straightforward measurement of the characteristic step size of the delay line.

The frequency domain representation of the calibration interferogram has given us the information necessary to undo the QRF frequency shifts for each frequency detected by the array. The envelope function necessary for antiapodization is obtained from the decay of the calibration interferogram in t_{LO}. Our preferred approach to extracting the interferogram envelope decay is a model-independent route using Fourier analysis. The FT of the real-valued calibration interferogram, Eq. (17), is taken. The negative frequency half of the data are replaced with zeros, and an inverse Fourier transform yields a complex calibration interferogram with the same information content as the original (equivalent to a Kramers–Kronig inversion) [26]. Computing the t_{LO}-dependent magnitude of this complex interferogram gives the envelope decay without the high-frequency oscillatory components. An independent envelope function can be obtained from the interferogram for each pixel simultaneously in this manner. In general, each pixel has a different response P_k, and the interval of frequencies detected is of a different length. Therefore the envelope functions necessary to antiapodize the interferograms collected at each pixel are generally not identical. As t_1 is scanned to acquire the signal interferogram for 2D IR, these envelopes decay as a function of $t_{\mathrm{LO}} = ft_1$. The envelope correction is demonstrated in Section 3.A.

3. EXPERIMENTAL DEMONSTRATION WITH 2D IR SPECTROSCOPY

The quasi-rotating frame technique along with its complementary calibration interferogram method have been implemented on two noncollinear (box-CARS geometry) ultrafast 2D IR spectroscopy systems. Example data have been obtained on both systems to illustrate the QRF method and compare the results to data on the same samples taken in the stationary frame. The systems have been described in depth previously [14,43–46], but the major differences between them will be summarized here. One system begins with relatively short pulses from a regeneratively amplified Ti:sapphire laser, typically less than 45 fs full width at half-maximum (FWHM), at 800 nm. The subsequent multistage optical parametric amplifier (OPA) outputs mid-IR pulses centered at about 4 μm with around 230 cm^{-1} FWHM bandwidth and duration

typically less than 65 fs. The excitation beams are focused into the sample, and the nonlinear signal is collimated, with a pair of gold off-axis parabolic mirrors. Most experiments, particularly those on broader resonances, use the 150 line/mm IR diffraction grating of the monochromator. The other system begins with considerably longer 90 fs pulses from the amplifier. The OPA generates mid-IR pulses centered at about 4.6 μm with narrower bandwidth of about 90 cm^{-1} and duration of about 120 fs. The three excitation beams are focused into the sample with independent lenses, and the signal is collimated by a fourth lens after the sample. A 300 line/mm grating is used in the monochromator for this system; narrower vibrational resonances are typically studied. The two 32-element mercury cadmium telluride (MCT) array detectors in use have similar pixel dimensions, with the same monochromators, giving about 6.3 cm^{-1} resolution (pixel-to-pixel frequency spacing) at 4 μm with the 150 line/mm grating and 1.4 cm^{-1} resolution at 4.6 μm with the 300 line/mm grating. Nonlinear signals are generated using the all-parallel polarization configuration, $\langle XXXX \rangle$.

A. Envelope Correction

In the subsequent comparisons of stationary and rotating frame 2D IR datasets, the apodization due to temporal walk-off between the signal and LO pulses was found to be an extremely minor effect for the experimental systems and instrumental configurations considered. Thus, while the calibration interferogram was used to determine the correct rotating frame frequencies with which to shift the ω_1 axes, the envelope correction (described in Section 2.D) was not performed on the source interferograms. Narrower resonances tend to have longer dephasing decays in t_1, but the 2D IR data tends to be acquired using higher line density gratings and therefore a smaller range of frequencies on each pixel. These two features counteract somewhat the effect of the LO envelope for interferograms that must be sampled for long t_1 ranges. For extremely long-lived t_1 decays or, in particular, samples that have a large inhomogeneous linewidth but a relatively narrow homogeneous linewidth, the correction could become significant at short t_2 (where only homogeneous dephasing remains in the rephasing pathway).

To demonstrate the envelope correction, our examples are 2D IR interferograms from a sample with a very small linewidth, isotopically labeled carbon dioxide ($^{13}CO_2$) at low concentration in the room temperature ionic liquid 1-ethyl-3-methylimidazolium bis(trifluoromethylsulfonyl) imide ($EmimNTf_2$) [47,48]. The absorption is centered at 2277 cm^{-1} with a FWHM of 5 cm^{-1}. This system has been investigated previously by polarization-selective pump-probe and 2D IR spectroscopy, but the 2D IR interferograms taken in a noncollinear geometry have not been presented before [47,48]. The short pulse system's output IR spectrum was tuned to the CO_2 absorption at 4.4 μm and the 300 line/mm grating was used.

We consider ω_3 at the peak frequency of 2277 cm^{-1} only for this example and fix the population time at $t_2 = 0.3$ ps. In general a different calibration interferogram, with a slightly distinct envelope, is recorded at each pixel. The results are shown in Figure 3. The LO delay was scanned between −50 and 50 ps,

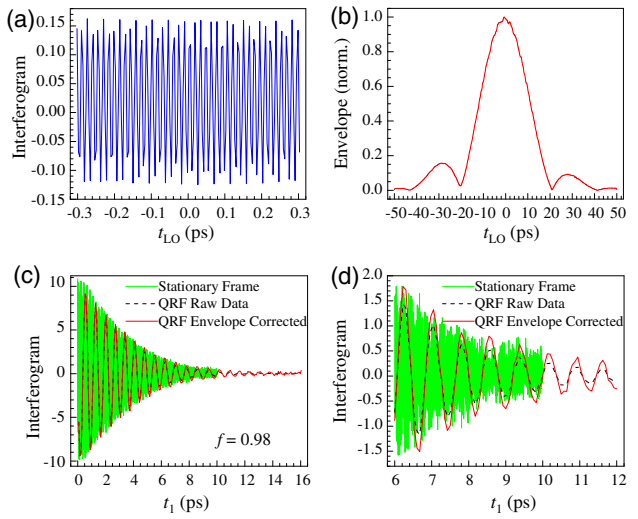

Fig. 3. Examples of the calibration interferogram and envelope correction applied to 2D IR rephasing interferograms. Pixel center frequency is 2277 cm^{-1}, the peak wavelength of the $^{13}CO_2$ asymmetric stretch in the ionic liquid $EmimNTf_2$. (a) Short delay time portion of the calibration interferogram with visible oscillations. The (constant) heterodyned signal is the third-order emitted field from CO_2; the local oscillator delay was scanned from −50 to 50 ps in 2 fs steps. (b) The interferogram envelope calculated from the full dataset of (a) as described in Section 2.D. (c) Rephasing interferogram of CO_2 in $EmimNTf_2$ at a waiting time of $t_2 = 0.3$ ps, shown over the full positive t_1 range. Data are shown for the stationary frame (green, solid line), quasi-rotating frame without envelope correction (black, dashed line), and corrected QRF data using the envelope in (b) (red, solid line). QRF used a fraction $f = 0.98$. (d) Same datasets as part (c), but focusing on the long-t_1 points to show more clearly the effect of the LO envelope decay and the application of the correction.

with 2 fs steps, to create the calibration interferogram (note that such a large range and dense sampling is not generally required; this calibration interferogram was taken specifically to illustrate the technique). In Fig. 3(a), a short portion of this data is shown around zero delay, displaying the high-frequency oscillations. The envelope of the interferogram was extracted as described in Section 2.D; it is shown in Fig. 3(b). The long t_{LO} delay range shows the decay of the envelope to very low values, with several apparent nulls. The envelope has a roughly |sinc| shape, as expected for a nearly rectangular pixel response that is narrower than the signal and LO spectra [Eq. (17)]. The nulls could lead to ambiguities in signal interferograms corrected with this envelope; only the range $-20 \text{ ps} \le t_{LO} \le 20$ ps, in this example, should be used for antiapodization.

Rephasing interferograms (i.e., $t_1 > 0$) of carbon dioxide in $EmimNTf_2$ are shown in Figs. 3(c) and 3(d). Figure 3(c) shows the full time range, while Fig. 3(d) displays only a selection of the longer delay time points. The stationary frame data is in green. Data taken with the QRF and a fraction $f = 0.98$ are shown in black (dashed line). Particularly at the longer times [Fig. 3(d)], the black interferogram envelope decays more rapidly than the green stationary frame one. Antiapodization with the envelope from the calibration interferogram [Fig. 3(b)] results in the red data (solid line). Figures 3(c) and 3(d) illustrate clearly that the corrected QRF interferogram (red) closely

matches the envelope decay of the stationary frame interferogram (green). Despite the visible difference in the interferograms at long time, the short time portion of the uncorrected QRF interferogram decay is barely distinguishable from that in the stationary frame. Antiapodization with the envelope does not greatly change the 2D line shapes obtained from fully processing these QRF interferograms across all the ω_3 values, but the CO_2 in the $EmimNTf_2$ system does provide a useful example of envelope correction with the calibration interferogram. Again, samples that have particularly narrow homogeneous linewidths compared to their inhomogeneous widths could show a greater dependence on the envelope correction.

B. Broadband 2D IR Spectroscopy with Short Pulses

To demonstrate the use of QRF detection for samples with extremely broad IR absorption resonances, our model system is bulk water. We study the O-D stretch of 5% HOD (singly deuterated water) in H_2O, produced through proton exchange by adding 2.5% D_2O to pure water. The linear absorption spectrum is centered at 2509 cm^{-1} with a FWHM of 160 cm^{-1} (Fig. 4). Spectral diffusion dynamics of HOD in H_2O have been obtained via 2D IR previously and analyzed in depth in terms of fluctuations and exchange in the water hydrogen bond network [3,39,49,50]. Here we are only concerned with comparing spectra taken on this same material but with different acquisition techniques.

2D IR experiments were conducted with the waiting time t_2 varying from 160 fs to 1.8 ps in both the stationary frame and the quasi-rotating frame with $f = 0.82$. The 2D line shapes were analyzed using the CLS-ω_3 technique to extract the waiting-time-dependent spectral diffusion dynamics [38]. This is the primary 2D IR feature of interest for understanding the ultrafast dynamics of systems with a single vibrational transition. Maintaining the correct line shape with different acquisition techniques is a stringent test—if the line shape is correct, it is almost guaranteed that other parameters of a 2D IR spectrum, such as the positions of various bands that reveal coupling constants for multioscillator systems, will be preserved as well. Such a comparison for 2D IR spectra taken in the stationary frame in a noncollinear geometry and the rotating frame with a pump-probe geometry pulse shaping system has shown that the line shape results are indistinguishable [22].

The results on HOD in H_2O are shown in Fig. 5. Figure 5(a) shows an example of a 2D spectrum taken using the QRF (and subsequently shifted back to the stationary frame) with $t_2 = 1$ ps. The upper, positive peak on the diagonal is the 0–1 transition, whose line shape we analyzed with the CLS method. The lower, negative peak is the 1–2 transition, which is shifted down in ω_3 by the vibrational anharmonicity. The small distortion in the 1–2 band around 2350 cm^{-1} is caused by incomplete purging of CO_2 from the experimental system. Comparison to previously reported 2D IR spectra of HOD in H_2O by Asbury *et al.* shows that the overall form of the correlation spectrum with QRF detection is identical to that obtained in a stationary frame experiment [39,49].

QRF and stationary frame CLS data points (normalized FFCF) for the 0–1 portion of the spectra are compared in

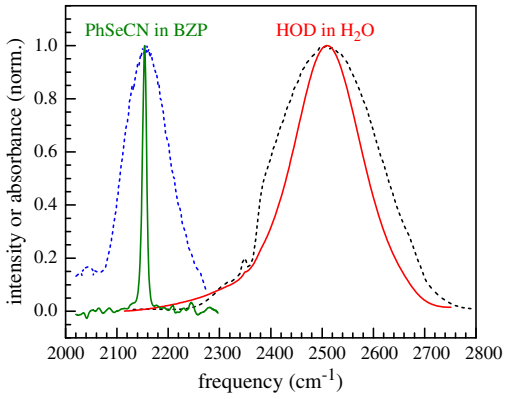

Fig. 4. Background-subtracted and normalized linear absorption spectra for HOD in bulk water (H_2O) and phenyl selenocyanate (PhSeCN) in benzophenone (BZP): solid red and green lines, respectively. Excitation laser spectra for the shorter pulse (black) and longer pulse (blue) systems, tuned to resonance with HOD and PhSeCN, respectively, are shown as dashed lines. The absorption in the shorter pulse spectrum around 2350 cm^{-1} is due to residual atmospheric CO_2 before complete purging of the spectrometer.

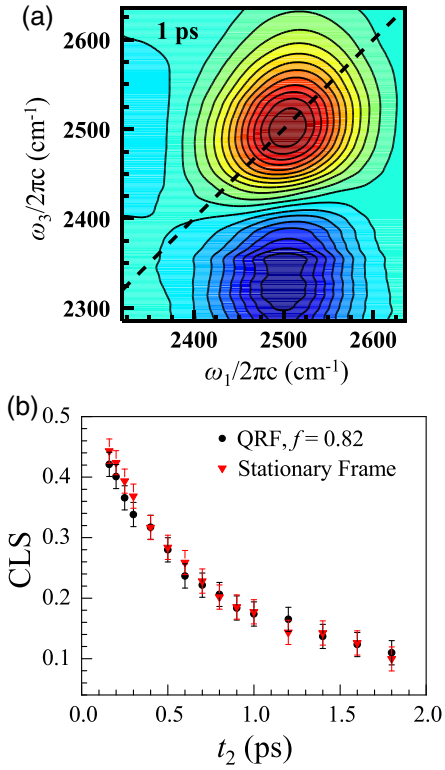

Fig. 5. Comparison of stationary frame and QRF 2D IR results for HOD in H_2O, a broad vibrational band. (a) QRF 2D spectrum ($f = 0.82$) data at waiting time $t_2 = 1$ ps after shifting to stationary frame with monochromator calibration results. The upper band on the diagonal (red, positive sign) is from the 0–1 vibrational transition. The lower band (blue, negative sign) arises from the 1–2 transition and is shifted on the ω_3 axis by the vibrational anharmonicity. The distortion in the 1–2 band at ~2350 cm^{-1} is caused from absorption by CO_2 in the air. (b) CLS decays from 2D spectra taken in the QRF (black circles) and in the stationary frame (red downward triangles). Within experimental error, the curves are identical and both yield the previously reported biexponential decay times.

Fig. 5(b). The CLS decays are identical within experimental error. Some small differences are visible, particularly at short times, but the differences are within the typical error expected between different datasets (e.g., taken on different days) for the same sample material. Both CLS curves fit well to a biexponential decay having time constants of 380 fs and 1.7 ps, as has been reported previously [3]. To obtain more confidence in the CLS values for a sample not previously characterized by 2D IR, several datasets should be averaged. When this is done, there are no systematic differences between the stationary and rotating frame results.

C. Narrower-Band 2D IR Spectroscopy with Longer Pulses

The second model system for demonstration of the QRF is phenyl selenocyanate (PhSeCN), a long-lived vibrational probe, dissolved at 2.5 mol. % in benzophenone, a glass-forming liquid. The vibrational mode of interest is the nitrile (CN) stretch of PhSeCN. Its linear absorption spectrum peaks at 2154 cm^{-1}, and the FWHM of the band is only 10 cm^{-1} (Fig. 4). This vibrational mode, with a linewidth well over 10 times narrower than that of HOD in bulk water, permits a distinct comparison of the stationary and quasi-rotating frames from that in Section 3.B. The 2D IR experiments on the PhSeCN in benzophenone system could be conducted with waiting times in the range from 0.5 to 150 ps because of the long vibrational lifetime of the CN stretch of PhSeCN [45]. The experiments were performed at 335 K, above the melting point of benzophenone.

Results of these studies in the stationary frame and with the QRF are shown in Fig. 6. Figure 6(a) shows a QRF ($f = 0.965$) 2D spectrum at a waiting time $t_2 = 8$ ps. Both the 0–1 (upper) and 1–2 (lower) transition regions of the spectrum are shown. The features in the 2D correlation spectrum do not appear different from data obtained in the stationary frame. The center line slope results in Fig. 6(b) show essentially perfect agreement between the stationary frame and QRF data throughout the entire t_2 range, including the decay of frequency correlation all the way to zero and the ~50 ps of zero slope following this.

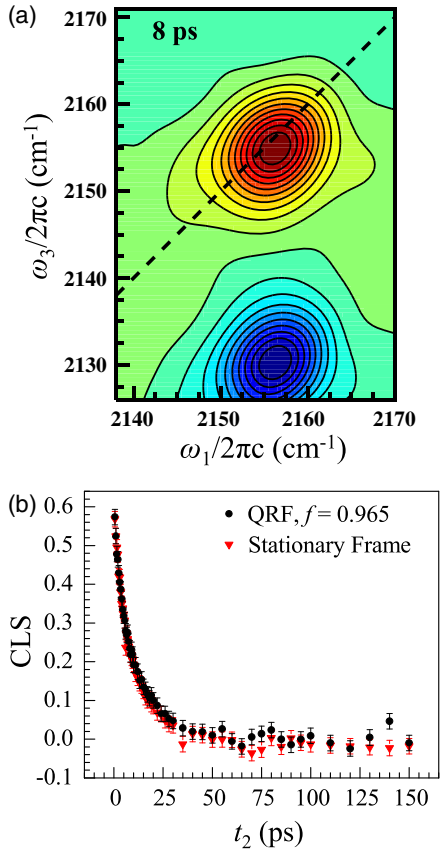

Fig. 6. Comparison of 2D IR results on phenyl selenocyanate in benzophenone, a narrower vibrational band, taken in both the stationary and rotating frames. (a) 2D spectrum taken with QRF ($f = 0.965$) at $t_2 = 8$ ps. The upper band on the diagonal is from the 0–1 vibrational transition. The lower band arises from the 1–2 transition and is shifted on the ω_3 axis by the vibrational anharmonicity. (b) CLS decays from the QRF 2D spectra (black circles) and stationary frame spectra (red downward triangles). The data are identical within experimental error.

D. Discussion

As we have demonstrated in Sections 3.B and 3.C, the QRF procedure allows acquisition of less densely sampled 2D IR interferograms without changing the results of line shape analysis procedures, such as the CLS that yield the dynamical information (FFCF) of the system. The ability of the QRF procedure to produce the correct time-dependent line shapes is a stringent test. In many applications, only peak positions or the time-dependent growth of peaks are of interest. Such measurements are less demanding than ones that require the correct shapes of the 2D bands. Therefore, the QRF procedure is widely applicable to 2D spectroscopy.

The visual appearance of the 2D spectral line shapes furthermore is not generally affected by the QRF method itself. However, we found that the noise characteristics of the 2D spectrometer and detection apparatus can become an important concern in choosing the rotating frame frequencies and sampling rate. The large bandwidth of the O-D stretch of HOD means it is more difficult to choose a region in ω_1 that is noise free, but also low in enough in frequency that a considerable reduction in sampling time is achieved by the QRF. Narrower bands such as the SeCN stretch (Section 3.C and Figs. 4 and 6) make this choice easier. If a noisy region is found, a small change in the f value can effectively move the entire spectral region of interest far enough from the noise that none of the 2D bands are distorted.

The width of the spectral region desired in ω_1 has other consequences for QRF detection. HOD in H_2O absorbs at a higher frequency; it extends on the blue side to about 2750 cm^{-1}. Conversely, the spectrum of PhSeCN in benzophenone does not even reach 2200 cm^{-1} (see Fig. 4). If only the absolute bandwidths (i.e., the range from zero to the highest frequency) were considered, it would appear that a greater efficiency increase is possible with rotating frame detection for the water system. However, the relative bandwidth occupied by the peak in ω_1 is much more important in determining how large a factor the sampling of the interferogram can be reduced by. The large relative bandwidth of HOD means a smaller f value must be used for the QRF; otherwise, there would be aliasing around zero frequency (Section 2.C).

Consider the examples in Sections 3.B and 3.C. For HOD, the lowest frequency collected in ω_3 is about 2290 cm^{-1}. The largest ω_1 frequency of 2750 cm^{-1} is shifted by $f\omega_3$ to 872 cm^{-1} at the reddest pixel by the rotating frame. In the narrowband example of PhSeCN, the lowest frequency collected is 2125 cm^{-1}. Its (overestimated) largest frequency in ω_1 of 2200 cm^{-1} is shifted at this pixel by $f\omega_3$ to about 150 cm^{-1}. Thus the QRF in these examples offers ~3.1-fold reduction in sampling for HOD, but a 14.7-fold reduction for PhSeCN. The stationary frame experiments on PhSeCN required approximately 15 min for each interferogram acquisition. With the QRF, the time is reduced to about 1 min. The CLS decays shown in Fig. 6(b) consist of 54 data points at different waiting times. The stationary frame experiments thus required about 13.5 h for a single repetition. Assuming the QRF calibration steps take around 1 h, and with 54 min of data acquisition, the same number of interferograms can be acquired in only 2 h total. Nearly 12 h of valuable instrument time could be saved considering just one repetition of the experiment, though more repetitions are taken in practice for additional signal averaging in the QRF scheme. The actual experiments, with additional averaging as necessary, took a total of 5 h in the QRF case and 21 h in the stationary frame case, in relatively good agreement with the simplified analysis above.

The massive difference in sampling reduction illustrated here means that the QRF can be much more beneficial for narrow lines, which also must be sampled to larger t_1 values. In addition to simply saving time by collecting a lower density of t_1 points, spending less time acquiring each full interferogram also means there is less opportunity for experimental instabilities, such as the drift of relative pulse timings, to occur. These instabilities can be encountered for very long t_1 scans such as required for CO_2 in ionic liquids (Fig. 3). Shortening the interferogram acquisition time with the QRF can be very useful in decreasing errors from experimental drifts.

While the experimental demonstrations in the present section have utilized 2D IR spectroscopy, the QRF methodology is equally applicable to multidimensional electronic spectroscopy in the visible or UV regimes. Considerations of the relative transition bandwidths will be quite important in anticipating the utility of (partially) rotating frame detection for these experiments. Electronic transition line shapes are typically much broader than vibrational bands. However, the absorptions are centered at higher absolute frequencies so the relative bandwidths are not necessarily greater than those in the IR.

4. QRF IMPLEMENTATION PROCEDURE

We assume the laser bandwidth and linear absorption spectrum of the sample under study are characterized (as in Fig. 4), so that the ω_1 and ω_3 ranges that may contain signal frequencies are known to the user. Briefly, the steps for implementing the QRF procedure are as follows.

1. Select the ω_3 range to be studied, with upper and lower bounds $\omega_{3,f}$ and $\omega_{3,i}$, respectively (Fig. 2).
2. Choose an initial QRF fraction f_i to minimize the frequencies in ω_1 while maintaining the inequality in Eq. (15) for the lowest initial oscillation frequency possible, $\omega_{1,i}$ (Fig. 2).

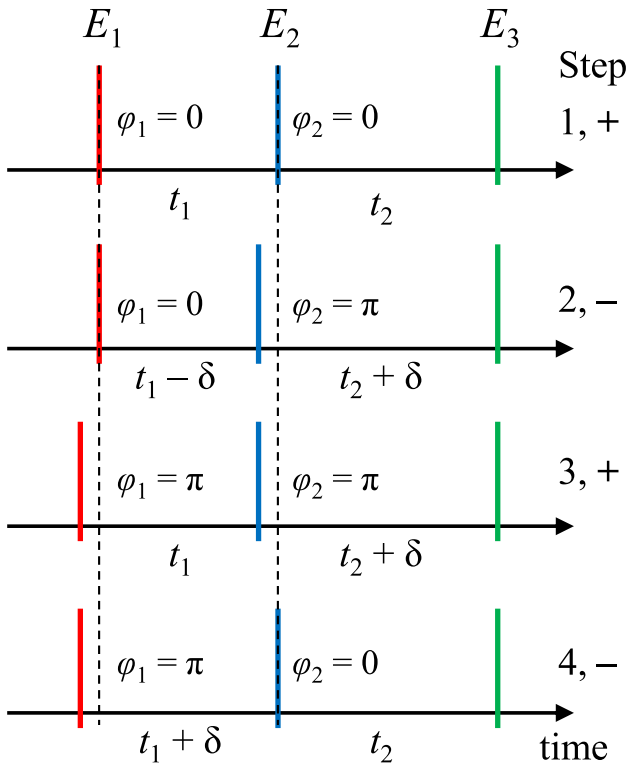

Fig. 7. Schematic timing diagram of the four-step quasi-phase-cycling procedure in use on the shorter pulse 2D IR system. Pulses 1, 2, and 3 (left to right) are visualized as red, blue, and green lines, respectively. The four steps are averaged for a block of laser shots (order of 100) at particular t_1 and t_2 values. At the chosen center frequency ω for QPC, $\delta = \pi/\omega$ is the half-cycle time step. A pulse delay by δ approximates a phase shift of π across the detected ω_1 frequency range. The approximate phases φ_1 and φ_2 of pulses 1 and 2 are shown at each step in the phase cycle, and the overall sign of each step (numbered 1–4) is given at the right. The abbreviated QPC procedure used on the narrow band system consists of only steps 1 and 4.

3. The largest initial oscillation frequency possible, $\omega_{1,f}$, becomes $\omega_{1,f} - f_i\omega_{3,i}$ at the reddest pixel (Fig. 2). Select a t_1 sampling rate to meet the Nyquist condition: at least two time points per cycle. The step size Δt_1 must be accessible by an integer number of delay line steps.
4. The actual QRF fraction f is calculated as the closest value to f_i such that $f\Delta t_1$ is also accessible by an integer step number.
5. Obtain a calibration interferogram over the t_{LO} range of interest (typically the whole t_1 range for the 2D experiment at minimum) at the ω_3 values for the actual experiment. Process the interferogram to obtain the pixel center frequencies ω_k and the signal-LO envelope decay (Section 2.D). Note: this step can be performed after the 2D experiment instead, or in addition as a consistency check.
6. Conduct the 2D optical spectroscopy experiment, collecting rotating frame interferograms at each ω_3. The LO pulse delay is varied as $t_{LO} = ft_1$ (time intervals as in Fig. 1; note that t_{LO} and t_1 become negative for the nonrephasing interferogram).
7. Process the interferograms, starting with t_1 Fourier transforms of the rephasing and nonrephasing data. Shift the ω_1 frequency axis by the rotating frame frequency $f\omega_k$ at each

pixel k, and trim the ω_1 range to retain only the region of interest (i.e., as would be processed in a stationary frame experiment). The interferograms should be zero padded for sufficient resolution in ω_1 that the frequency shifts by $f\omega_k$ can be approximated by integer multiples of the point spacing. Note: this approach avoids the necessity to interpolate time-domain interferograms (which are generally sampled below the Nyquist limit for the stationary frame) to apply a time-dependent phase factor to accomplish the frequency shift.

8. The rephasing and nonrephasing raw 2D spectra are now in the stationary frame and can be processed with the normal procedures (e.g., phase corrections [14,36]) necessary to obtain absorptive 2D spectra for analysis [15,17].

5. CONCLUDING REMARKS

We have introduced a new technique for improving the sampling efficiency of time-domain interferograms necessary for noncollinear 2D optical spectroscopy, the quasi-rotating frame. Procedures to shift the data into the rotating frame for acquisition and then to return the results to the stationary frame for analysis, using a calibration interferogram, were described in detail. Executing the QRF procedure and calibration scans requires only software changes in many existing noncollinear 2D spectrometers, because the local oscillator delay is typically precisely controllable in these instruments. The QRF adds local oscillator delay steps along with the scanning of pulse 1 or 2 in the collection of interferograms. Potential problems introduced by QRF detection were identified, and straightforward solutions were described to avoid distortion of the 2D line shapes.

Two model systems were discussed for a comparison of the 2D line shapes acquired in the stationary and rotating frames, HOD in H_2O and phenyl selenocyanate in benzophenone. The O-D stretch of HOD is a very broad IR band, while the nitrile stretch of phenyl selenocyanate is relatively narrow. Center line slope analysis to extract the normalized frequency–frequency correlation function, which quantifies spectral diffusion, was performed on the spectra. The CLS decays are essentially identical for the stationary and rotating frame spectra, both for narrow bands and broad bands. Thus, quantitative line shape analysis can be conducted on these rapidly acquired spectra to extract the detailed dynamics of liquid structural evolution.

We found that the QRF can offer a much greater efficiency improvement (larger factor of sampling reduction) for the narrow-band example system, because the smaller relative bandwidth of its spectrum allows it to be shifted closer to zero frequency, that is, a more rapidly rotating frame (larger f fraction). It is these experimental systems that are in greater need of an efficiency improvement, because each interferogram can take a substantial amount of time to acquire with full sampling of the interferogram in the stationary frame.

APPENDIX A: QUASI-PHASE-CYCLING ROUTINES FOR SCATTER REMOVAL OR CHOPPER-FREE ACQUISITION

Phase cycling has been a highly successful approach to selecting the desired signals over various artifacts, first in NMR [20,51] and more recently in nonlinear optical spectroscopy [13,21–23,51,52]. QPC has previously been demonstrated in 2D IR spectroscopy by Bloem *et al.*, using both wobbling Brewster windows and photoelastic modulators to variably delay one or more of the excitation pulses in sync with the laser repetition rate [37]. Subcycle pulse delays approximate phase shifts and can therefore be used to phase cycle perfectly at a single frequency and with only small error over ranges of several hundred wavenumbers around this chosen center [21,37]. Thus, QPC can be used to acquire third-order signal and cancel the interference from scattered light, all without the use of a chopper. If the dynamics of the system in the nonlinear optical response's coherence and population periods do not evolve rapidly on the time scale of a half cycle of light, pulse delays of approximately half a cycle can be assumed to vary only the phase of the third-order signal and not the sampling of the response function. This approximation has been shown to be a good one for 2D IR spectroscopy by Bloem *et al.* [37].

If the sources of scatter are somewhat rapidly varying, then adjusting the phase on each laser shot is optimal for removing these artifacts, which often appear on the diagonal in the 2D spectrum and interfere with line shape analysis. In the case of QRF detection, however, relatively static scatter becomes a problem for detection if it oscillates due to the local oscillator's variable delays. Fast phase cycling is not necessary to remove this scatter contribution; the precision delay lines can vary the phase of the signal averaged for a few hundred shots at a time (at 1 kHz laser repetition rate, a few hundred milliseconds) by making approximately half-cycle steps. The LO spectrum is similarly a slowly varying contribution to the total detected signal. Quasi-phase-cycling with the delay lines over blocks of laser shots can select for either the heterodyne signal or the LO contribution alone based on the linear combination of different data phases. Thus 2D IR data can be acquired without a chopper while still removing scatter and LO background contributions.

The simplest QPC scheme of this variety was used with a chopper to remove the "systematic" 3-LO scatter term on the narrow-band system used to obtain the data shown in Fig. 6. The pulse that is being scanned for a particular pathway (1 for rephasing, 2 for nonrephasing) is alternatively offset by zero or π in phase at the relevant center frequency, and several hundred shots are acquired. If the chosen center is ω, the half-cycle delay time is defined as $\delta = \pi/\omega$. The π-phase average is subtracted from the zero-phase average. This doubles the signal, which flips in phase with the scanned pulse, and cancels the pulse 3–LO scatter cross term, which does not depend on the phase of pulses 1 or 2. Because this scheme cannot remove many scatter contributions, such as those involving the scanned pulse, a chopper is mandatory to avoid further artifacts.

On the short-pulse 2D IR system, a four-step quasi-phase-cycle was used that is analogous to the four-shot phase cycling scheme commonly employed in pulse shaping 2D IR systems [22]. Of the three excitation pulses, pulses 1 and 2 are controllable by precision delay stages (like the arbitrarily shaped initial pulse pair in a pulse shaping system). The approximate phases of the first and second pulse to arrive at the sample (1, 2 for rephasing and 2, 1 for nonrephasing), φ_1 and φ_2, are varied as $(0, 0)$, $(0, \pi)$, (π, π), and $(\pi, 0)$. The four steps of the cycle are illustrated schematically in Fig. 7. Each step is acquired for a

block of laser shots at a particular t_1 and t_2 point, and the results are linearly combined to quadruple the signal. Steps 1 and 3 have positive sign while steps 2 and 4 have negative sign, as determined by the relative phase of pulses 1 and 2.

The phase cycle given in Fig. 7 is easy to implement because each step requires only one delay line move. If multiple delay lines can be moved simultaneously, of course, the steps can be acquired in any desired order in the same amount of time. The waiting time, t_2, has an average value of $t_2 + \delta/2$ throughout the cycle. This is not expected to be noticeable, because a half-cycle delay δ (less than 8 fs for our vibrational probe examples) is extremely short on the time scale of liquid fluctuation dynamics. The average of t_1, on the other hand, is not altered by the phase cycle. To first order in this coherence time, the sampling of the response function is unchanged.

Chopping removes scatter terms that do not depend on pulse 3, and the four-step phase cycle removes scatter terms that do not depend on both pulses 1 and 2. Chopping and QPC together can remove almost the entirety of the scatter (often referred to as an "8-shot" scheme with shot-by-shot phase cycling) [37,53,54]. If the pulse 1–pulse 2 scatter cross term is not large and scatter amplitude does not vary with a similar time scale to the length of one phase cycle step, this QPC procedure alone can acquire accurate 2D IR spectra without the use of chopping, nearly doubling the duty cycle of the instrument because all laser shots result in nonlinear signal, as opposed to half of the shots with chopping. The LO spectrum (for normalization of the heterodyne signal) is accessible from the same four phase steps by adding all four with positive sign.

In particular, the QRF with QPC can be performed without a chopper because the phase cycle removes the cross terms from all three excitation pulses contributing scatter that is heterodyned by the local oscillator. However, caution is necessary regarding the 1–2 scatter cross term: if large enough to be detected (less likely on noncollinear setups than in the pump-probe geometry) it will be aliased into the spectral region sampled by QPC and may overlap the desired peaks.

Funding. U.S. Department of Energy (DOE) (DE-FG03-84ER13251); Air Force Office of Scientific Research (AFOSR) (FA9550-16-1-0104); National Science Foundation (NSF) (CHE-1461477).

Acknowledgment. We thank Jun Nishida for many stimulating discussions. P. L. K. and A. T. acknowledge partial support from Stanford Graduate Fellowships and K. P. S. from an ARCS fellowship. DOE Grant DE-FG03-84ER13251 supported P. L. K., C. H. G., and the shorter-pulse 2D IR spectrometer. AFOSR Grant FA9550-16-1-0104 supported A. T. NSF Grant CHE-1461477 supported D. J. H., K. P. S., and the narrower-band 2D IR spectrometer.

REFERENCES

1. S. Mukamel, *Principles of Nonlinear Optical Spectroscopy* (Oxford University, 1995).
2. S. T. Roberts, J. J. Loparo, and A. Tokmakoff, "Characterization of spectral diffusion from two-dimensional line shapes," J. Chem. Phys. **125**, 084502 (2006).
3. S. Park, D. E. Moilanen, and M. D. Fayer, "Water dynamics-the effects of ions and nanoconfinement," J. Phys. Chem. B **112**, 5279–5290 (2008).
4. E. T. J. Nibbering and T. Elsaesser, "Ultrafast vibrational dynamics of hydrogen bonds in the condensed phase," Chem. Rev. **104**, 1887–1914 (2004).
5. R. A. Nicodemus, S. A. Corcelli, J. L. Skinner, and A. Tokmakoff, "Collective hydrogen bond reorganization in water studied with temperature-dependent ultrafast infrared spectroscopy," J. Phys. Chem. B **115**, 5604–5616 (2011).
6. R. A. Nicodemus, K. Ramasesha, S. T. Roberts, and A. Tokmakoff, "Hydrogen bond rearrangements in water probed with temperature-dependent 2D IR," J. Phys. Chem. Lett. **1**, 1068–1072 (2010).
7. H. J. Bakker and J. L. Skinner, "Vibrational spectroscopy as a probe of structure and dynamics in liquid water," Chem. Rev. **110**, 1498–1517 (2010).
8. P. L. Geissler, "Water interfaces, solvation, and spectroscopy," Annu. Rev. Phys. Chem. **64**, 317–337 (2013).
9. D. M. Jonas, "Two-dimensional femtosecond spectroscopy," Annu. Rev. Phys. Chem. **54**, 425–463 (2003).
10. T. Brixner, J. Stenger, H. M. Vaswani, M. Cho, and G. R. Fleming, "Two-dimensional spectroscopy of electronic couplings in photosynthesis," Nature **434**, 625–628 (2005).
11. C. Consani, G. Auböck, F. van Mourik, and M. Chergui, "Ultrafast tryptophan-to-heme electron transfer in myoglobins revealed by UV 2D spectroscopy," Science **339**, 1586–1589 (2013).
12. N. Krebs, I. Pugliesi, J. Hauer, and E. Riedle, "Two-dimensional Fourier transform spectroscopy in the ultraviolet with sub-20 fs pump pulses and 250–720 nm supercontinuum probe," New J. Phys. **15**, 085016 (2013).
13. P. Hamm and M. T. Zanni, *Concepts and Methods of 2D Infrared Spectroscopy* (Cambridge University, 2011).
14. S. Park, K. Kwak, and M. D. Fayer, "Ultrafast 2D-IR vibrational echo spectroscopy: a probe of molecular dynamics," Laser Phys. Lett. **4**, 704–718 (2007).
15. S. M. Gallagher Faeder and D. M. Jonas, "Two-dimensional electronic correlation and relaxation spectra: theory and model calculations," J. Phys. Chem. A **103**, 10489–10505 (1999).
16. S. M. Gallagher, A. W. Albrecht, T. D. Hybl, B. L. Landin, B. Rajaram, and D. M. Jonas, "Heterodyne detection of the complete electric field of femtosecond four-wave mixing signals," J. Opt. Soc. Am. B **15**, 2338–2345 (1998).
17. M. Khalil, N. Demirdoven, and A. Tokmakoff, "Obtaining absorptive line shapes in two-dimensional infrared vibrational correlation spectra," Phys. Rev. Lett. **90**, 047401 (2003).
18. M. Khalil, N. Demirdoven, and A. Tokmakoff, "Coherent 2D IR spectroscopy: molecular structure and dynamics in solution," J. Phys. Chem. A **107**, 5258–5279 (2003).
19. C. Scheurer and S. Mukamel, "Magnetic resonance analogies in multidimensional vibrational spectroscopy," Bull. Chem. Soc. Jpn. **75**, 989–999 (2002).
20. J. Keeler, *Understanding NMR Spectroscopy*, 2nd ed. (Wiley, 2010).
21. A. W. Albrecht, J. D. Hybl, S. M. Gallagher Faeder, and D. M. Jonas, "Experimental distinction between phase shifts and time delays: implications for femtosecond spectroscopy and coherent control of chemical reactions," J. Chem. Phys. **111**, 10934–10956 (1999).
22. S. K. Karthick Kumar, A. Tamimi, and M. D. Fayer, "Comparisons of 2D IR measured spectral diffusion in rotating frames using pulse shaping and in the stationary frame using the standard method," J. Chem. Phys. **137**, 184201 (2012).
23. S.-H. Shim and M. T. Zanni, "How to turn your pump-probe instrument into a multidimensional spectrometer: 2D IR and Vis spectroscopies via pulse shaping," Phys. Chem. Chem. Phys. **11**, 748–761 (2009).
24. C. W. Hillegas, J. X. Tull, D. Goswami, D. Strickland, and W. S. Warren, "Femtosecond laser pulse shaping by use of microsecond radio-frequency pulses," Opt. Lett. **19**, 737–739 (1994).
25. M. R. Fetterman, D. Goswami, D. Keusters, W. Yang, J. K. Rhee, and W. S. Warren, "Ultrafast pulse shaping: amplification and characterization," Opt. Express **3**, 366–375 (1998).

26. J. A. Myers, K. L. M. Lewis, P. F. Tekavec, and J. P. Ogilvie, "Two-color two-dimensional Fourier transform electronic spectroscopy with a pulse-shaper," Opt. Express **16**, 17420–17428 (2008).
27. J. D. Hybl, A. A. Ferro, and D. M. Jonas, "Two-dimensional Fourier transform electronic spectroscopy," J. Chem. Phys. **115**, 6606–6622 (2001).
28. T. Brixner, T. Mancal, I. V. Stiopkin, and G. R. Fleming, "Phase-stabilized two-dimensional electronic spectroscopy," J. Chem. Phys. **121**, 4221–4236 (2004).
29. E. Harel, A. F. Fidler, and G. S. Engel, "Real-time mapping of electronic structure with single-shot two-dimensional electronic spectroscopy," Proc. Natl. Acad. Sci. USA **107**, 16444–16447 (2010).
30. E. Harel, A. F. Fidler, and G. S. Engel, "Single-shot gradient-assisted photon echo electronic spectroscopy," J. Phys. Chem. A **115**, 3787–3796 (2011).
31. P. D. Dahlberg, A. F. Fidler, J. R. Caram, P. D. Long, and G. S. Engel, "Energy transfer observed in live cells using two-dimensional electronic spectroscopy," J. Phys. Chem. Lett. **4**, 3636–3640 (2013).
32. V. P. Singh, A. F. Fidler, B. S. Rolczynski, and G. S. Engel, "Independent phasing of rephasing and non-rephasing 2D electronic spectra," J. Chem. Phys. **139**, 084201 (2013).
33. M. L. Cowan, J. P. Ogilvie, and R. J. D. Miller, "Two-dimensional spectroscopy using diffractive optics based phased-locked photon echoes," Chem. Phys. Lett. **386**, 184–189 (2004).
34. U. Selig, F. Langhojer, F. Dimler, T. Löhrig, C. Schwarz, B. Gieseking, and T. Brixner, "Inherently phase-stable coherent two-dimensional spectroscopy using only conventional optics," Opt. Lett. **33**, 2851–2853 (2008).
35. I. A. Heisler, R. Moca, F. V. A. Camargo, and S. R. Meech, "Two-dimensional electronic spectroscopy based on conventional optics and fast dual chopper data acquisition," Rev. Sci. Instrum. **85**, 063103 (2014).
36. D. E. Moilanen, "Water dynamics near solutes and surfaces," Ph.D. thesis (Stanford University, 2009).
37. R. Bloem, S. Garrett-Roe, H. Strzalka, P. Hamm, and P. Donaldson, "Enhancing signal detection and completely eliminating scattering using quasi-phase-cycling in 2D IR experiments," Opt. Express **18**, 27067–27078 (2010).
38. K. Kwak, D. E. Rosenfeld, and M. D. Fayer, "Taking apart the two-dimensional infrared vibrational echo spectra: more information and elimination of distortions," J. Chem. Phys. **128**, 204505 (2008).
39. J. B. Asbury, T. Steinel, K. Kwak, S. A. Corcelli, C. P. Lawrence, J. L. Skinner, and M. D. Fayer, "Dynamics of water probed with vibrational echo correlation spectroscopy," J. Chem. Phys. **121**, 12431 (2004).
40. J. R. Schmidt, S. A. Corcelli, and J. L. Skinner, "Pronounced non-Condon effects in the ultrafast infrared spectroscopy of water," J. Chem. Phys. **123**, 044513 (2005).
41. H.-S. Tan, "Theory and phase-cycling scheme selection principles of collinear phase coherent multi-dimensional optical spectroscopy," J. Chem. Phys. **129**, 124501 (2008).
42. K. Kwak, S. Park, I. J. Finkelstein, and M. D. Fayer, "Frequency–frequency correlation functions and apodization in two-dimensional infrared vibrational echo spectroscopy: a new approach," J. Chem. Phys. **127**, 124503 (2007).
43. P. L. Kramer, C. H. Giammanco, and M. D. Fayer, "Dynamics of water, methanol, and ethanol in a room temperature ionic liquid," J. Chem. Phys. **142**, 212408 (2015).
44. E. E. Fenn, D. B. Wong, and M. D. Fayer, "Water dynamics in small reverse micelles in two solvents: two-dimensional infrared vibrational echoes with two-dimensional background subtraction," J. Chem. Phys. **134**, 054512 (2011).
45. K. P. Sokolowsky, H. E. Bailey, and M. D. Fayer, "New divergent dynamics in the isotropic to nematic phase transition of liquid crystals measured with 2D IR vibrational echo spectroscopy," J. Chem. Phys. **141**, 194502 (2014).
46. I. J. Finkelstein, J. Zheng, H. Ishikawa, S. Kim, K. Kwak, and M. D. Fayer, "Probing dynamics of complex molecular systems with ultrafast 2D IR vibrational echo spectroscopy," Phys. Chem. Chem. Phys. **9**, 1533–1549 (2007).
47. C. H. Giammanco, P. L. Kramer, S. A. Yamada, J. Nishida, A. Tamimi, and M. D. Fayer, "Coupling of carbon dioxide stretch and bend vibrations reveals thermal population dynamics in an ionic liquid," J. Phys. Chem. B **120**, 549–556 (2016).
48. C. H. Giammanco, P. L. Kramer, S. A. Yamada, J. Nishida, A. Tamimi, and M. D. Fayer, "Carbon dioxide in an ionic liquid: structural and rotational dynamics," J. Chem. Phys. **144**, 104506 (2016).
49. J. B. Asbury, T. Steinel, C. Stromberg, S. A. Corcelli, C. P. Lawrence, J. L. Skinner, and M. D. Fayer, "Water dynamics: vibrational echo correlation spectroscopy and comparison to molecular dynamics simulations," J. Phys. Chem. A **108**, 1107–1119 (2004).
50. S. A. Corcelli, C. P. Lawrence, J. B. Asbury, T. Steinel, M. D. Fayer, and J. L. Skinner, "Spectral diffusion in a fluctuating charge model of water," J. Chem. Phys. **121**, 8897–8900 (2004).
51. D. Keusters, H.-S. Tan, and Warren, "Role of pulse phase and direction in two-dimensional optical spectroscopy," J. Phys. Chem. A **103**, 10369–10380 (1999).
52. P. Tian, D. Keusters, Y. Suzaki, and W. S. Warren, "Femtosecond phase-coherent two-dimensional spectroscopy," Science **300**, 1553–1555 (2003).
53. J. Nishida, A. Tamimi, H. Fei, S. Pullen, S. Ott, S. M. Cohen, and M. D. Fayer, "Structural dynamics inside a functionalized metal-organic framework probed by ultrafast 2D IR spectroscopy," Proc. Natl. Acad. Sci. USA **111**, 18442–18447 (2014).
54. C. R. Baiz, D. Schach, and A. Tokmakoff, "Ultrafast 2D IR microscopy," Opt. Express **22**, 18724–18735 (2014).